Numerical study of heat transfer in laminar and turbulent pipe flow with finite-size spherical particles

Mehdi Niazi Ardekani[*,a], Léa Al Asmar[b], Francesco Picano[c], Luca Brandt[a]

[a] Linné Flow Centre and SeRC (Swedish e-Science Research Centre), KTH Mechanics, Stockholm, SE-10044, Sweden
[b] Engineering Department, Sorbonne Universités, UPMC Univ Paris 06, UFR 919, Paris, F-75005, France
[c] Department of Industrial Engineering, University of Padova, Via Venezia 1, Padua, 35131, Italy

ABSTRACT

Controlling heat and mass transfer in particulate suspensions has many applications in fuel combustion, food industry, pollution control and life science. We perform direct numerical simulations (DNS) to study the heat transfer within a suspension of neutrally buoyant, finite-size spherical particles in laminar and turbulent pipe flows, using the immersed boundary method (IBM) to account for the solid fluid interactions and a volume of fluid (VoF) method to resolve the temperature equation both inside and outside the particles. Particle volume fractions up to 40% are simulated for different pipe to particle diameter ratios. We show that a considerable heat transfer enhancement (up to 330%) can be achieved in the laminar regime by adding spherical particles. The heat transfer is observed to increase significantly as the pipe to particle diameter ratio decreases for the parameter range considered here. Larger particles are found to have a greater impact on the heat transfer enhancement than on the wall-drag increase. In the turbulent regime, however, only a transient increase in the heat transfer is observed and the process decelerates in time below the values in single-phase flows as high volume fractions of particles laminarize the core region of the pipe. A heat transfer enhancement, measured with respect to the single phase flow, is only achieved at volume fractions as low as 5% in a turbulent flow.

1. Introduction

Heat transfer in particulate suspensions is a rather common process in many industrial and environmental areas such as fuel combustion, food industry, pollution control and life science. Many industrial examples support the importance of heat transfer among the two phases (Zonta et al., 2008), thus, the understanding and the ability to predict the heat exchange in wall-bounded suspensions has been of interest among the researchers for many decades (Guha, 2008). Predicting the heat transfer requires a knowledge of how particles are distributed across a wall-bounded domain, how particles affect the flow field and finally how they affect the heat transfer within the suspension. Answering these questions is even more complicated in turbulent suspensions where the presence of finite-size particles modulates the turbulence structures (Naso and Prosperetti, 2010). Inertial effects at the particle scale, yet in laminar flows, are shown to induce modifications of the suspension microstructure and to create a local anisotropy responsible for shear-thickening (Kulkarni and Morris, 2008; Picano et al., 2013), thus to a change of the macroscopic suspension dynamics. Shear-thickening and particle migration towards regions of low shear

has been documented in several studies in the literature for dense and dilute suspensions at low Reynolds numbers (Hampton et al., 1997; Brown and Jaeger, 2009; Yeo and Maxey, 2011; Guazzelli and Morris, 2011; Lashgari et al., 2017).

More in general, considering only the multiphase flow problem, Lashgari et al. (2014, 2016) documented the existence of three different regimes when changing the volume fraction ϕ of neutrally-buoyant spherical particles and the Reynolds number Re: a laminar-like regime at low Re and low to intermediate ϕ where the viscous stress dominates dissipation, a turbulent-like regime at high Reynolds number and low to intermediate ϕ where the turbulent Reynolds stress plays the main role in the momentum transfer across the channel and a third regime at higher ϕ, denoted as inertial shear-thickening, characterised by a significant enhancement of the wall shear stress due to the particle-induced stresses. Many studies have been dedicated in the recent years to the turbulence modulation in the presence of solid particles. A decrease of the critical Reynolds number for transition to turbulence is reported (Matas et al., 2003; Loisel et al., 2013; Yu et al., 2013; Lashgari et al., 2015) for semi-dilute suspensions of neutrally-buoyant spherical particles, whereas an enhancement of the turbulence activity is

---

documented at low volume fraction (up to 10%) Picano et al. (2015); Costa et al. (2016). Conversely, turbulence attenuation is observed at higher volume fractions in suspensions of spherical particles (Picano et al., 2015) and for spheroidal particles also at lower volume fractions (Ardekani et al., 2017; Eshghinejadfard et al., 2017).

Heat transfer studies in the laminar regime date back to the experiments of Ahuja (1975) on sheared suspensions of polystyrene particles at finite particle Reynolds number ($Re_p > 1$); the author attributed the enhancement of heat transfer to a mechanism based on inertial effects in which the fluid around the particle is centrifuged by the particle rotation. These experiments revealed that, increasing the shear rate, particle concentration and particle size increases the thermal conductivity of the suspension. Shin and Lee (2000) experimentally studied the heat transfer of suspensions with low volume fractions (up to 10%) for different shear rates and particle sizes. They found that the heat transfer increases with shear rate and particle size, however, it saturates at large shear rates. Recently, Ardekani et al. (2018) numerically investigated the effect of particle inertia, volume fraction and thermal diffusivity ratio on the heat transfer in Couette flow suspensions of spherical particles. They revealed that inertia at the particle scale induces a non-linear increase of the heat transfer as a function of the volume fraction, unlike the case at vanishing inertia where heat transfer increases linearly (Metzger et al., 2013).

Heat transfer in non-isothermal particle-laden turbulent flows has been the subject of many studies in the recent years. Heat transfer between the two phases and the alteration of heat transfer efficiency are investigated in Namburu et al. (2009); Chang et al. (2011); Bu et al. (2013). Avila and Cervantes (1995), used a Lagrangian-stochastic-deterministic model (LSD) to show that high mass loadings of small particles increases the heat transfer rate, while at low mass loadings, the heat transfer rate decreases. Particle size effect is investigated in Zonta et al. (2008); Hetsroni et al. (2002), who show that larger particles increase the heat transfer coefficient more significantly than smaller ones by using a two-way coupling approximation. Kuerten et al. (2011) performed two-way coupling simulations of turbulent channel flow, showing an enhancement of the heat transfer and a small increase in the friction velocity in the presence of heavy inertial particles with high specific heat capacity. Liu et al. (2017) investigated the effect of the particle heat capacity by a point-particle model approximation and report that the heat transfer reduces when large inertial particles with low specific heat capacity are added to the flow.

Despite all the work on this subject, a complete study on the effect of particle size (for finite-size particles) and volume fraction on heat transfer in pipe flows is still missing in the literature. Here, we therefore perform direct numerical simulations of heat transfer in laminar and turbulent suspensions with neutrally buoyant, finite-size spherical particles in a cylindrical pipe up to 40% volume fractions. We hope that this study lays the ground for further parameter studies in this complex subject.

The paper is organised as follows. The governing equations, numerical methods and the flow geometry are introduced in Section 2, followed by the results of the numerical simulations in Section 3. Main conclusions and final remarks are drawn in Section 4.

2. Methodology

2.1. Governing equations

The flow of an incompressible fluid is described by the Navier–Stokes equations:

$$\rho_f \left(\frac{\partial \mathbf{u}}{\partial t} + \mathbf{u} \cdot \nabla \mathbf{u} \right) = -\nabla p + \mu_f \nabla^2 \mathbf{u} + \rho_f \mathbf{f}, \tag{1}$$

$$\nabla \cdot \mathbf{u} = 0. \tag{2}$$

with $\mathbf{u}$ the fluid velocity, p the pressure, ρ_f the fluid density and μ_f the

dynamic viscosity of the fluid. The buoyancy effects are neglected in this work since the Grashof number, Gr, is considered to be small compared to the Reynolds number, Re for the studied cases. The ratio, Gr/Re^2, can be used as a measure for the importance of natural convection (Incropera et al., 2007). In addition, small temperature differences are assumed so as to neglect density variations inside the fluid, thus allowing us to focus on the role of particle size and volume fraction. The additional term $\mathbf{f}$ is added on the right-hand-side of Eq. (1) to account for the presence of particles, modelled with the immersed boundary method (IBM). This IBM force is active in the immediate vicinity of a particle and at the pipe wall in the present implementation to impose the no-slip and no-penetration boundary conditions indirectly (see the description of the numerical algorithm below).

The motion of neutrally buoyant rigid spherical particles is described by the Newton-Euler Lagrangian equations,

$$\rho_p V_p \frac{d\mathbf{U}_p}{dt} = \oint_{\partial S_p} \tau \cdot \mathbf{n} dA - V_p \nabla p_e + \mathbf{F}_c, \tag{3}$$

$$\mathbf{I}_p \frac{d\boldsymbol{\omega}_p}{dt} = \oint_{\partial S_p} \mathbf{r} \times (\tau \cdot \mathbf{n}) dA + \mathbf{T}_c, \tag{4}$$

with $\mathbf{U}_p$ and $\boldsymbol{\omega}_p$ the translational and the angular velocity of the particle. ρ_p, V_p and $\mathbf{I}_p$ are the particle mass density, volume and moment-of-inertia. The outward unit normal vector at the particle surface is denoted by $\mathbf{n}$ and $\mathbf{r}$ is the position vector from the particle center.

The integral of the stress tensor $\tau = -p\mathbf{I} + \mu_f(\nabla \mathbf{u} + \nabla \mathbf{u}^T)$ on the surface of particles accounts for the fluid-solid interactions, which are calculated by the IBM (see the description of the numerical algorithm below), while $V_p \nabla p_e$ in the expression above describes the external constant pressure gradient, used to drive the pipe flow at constant bulk velocity. $\mathbf{F}_c$ and $\mathbf{T}_c$ are the force and the torque, acting on the particles, due to the particle-particle (particle-wall) collisions.

The energy equation for incompressible flows can be simplified to:

$$\rho C_p \left[\frac{\partial T}{\partial t} + \mathbf{u} \cdot \nabla T \right] = \nabla \cdot (k \nabla T), \tag{5}$$

where C_p and k are the specific heat capacity and thermal conductivity, and T the temperature. We have considered the same ρC_p for the fluid and particles $((\rho C_p)_p = (\rho C_p)_f)$ in this study and thus Eq. (5) reduces to:

$$\frac{\partial T}{\partial t} + \mathbf{u} \cdot \nabla T = \nabla \cdot (\alpha \nabla T), \tag{6}$$

where α is the thermal diffusivity, $\alpha = k/(\rho C_p)$.

Eq. (6) is resolved on every grid point in the computational domain, i.e. in the fluid and solid phases.

2.2. Numerical algorithm

Uhlmann (2005) developed a computationally efficient immersed boundary method (IBM) to fully resolve particle-laden flows. Breugem (2012) introduced improvements to this method, making it second order accurate in space while increasing the numerical stability of the method for mass density ratios (particle over fluid density ratio) near unity (see also Kempe and Fröhlich, 2012). Ardekani et al. (2018) coupled the IBM with a volume of fluid (VoF) approach (Hirt and Nichols, 1981; Ström and Sasic, 2013) to study the heat transfer in a suspension of rigid particles. In this numerical scheme, the IBM accounts for fluid-solid interactions and by computing the local volume fraction of the solid phase a VoF approach is employed to solve the temperature equation in the two phases where different thermal diffusivities can be considered. Details on the IBM, accounting for fluid-solid interactions are discussed in Breugem (2012) with several validations reported in Lambert et al. (2013); Picano et al. (2015); Lashgari et al. (2016); Ardekani et al. (2016). For clarity a short description of the IBM is given in this section, followed by the VoF method used for the heat transfer within the suspension.

The flow field is resolved on a uniform ($\Delta x = \Delta y = \Delta z$), staggered, Cartesian grid while particles are represented by a set of Lagrangian points, uniformly distributed on the surface of each particle. The number of Lagrangian grid points N_L on the surface of each particle is defined such that the Lagrangian grid volume ΔV_l becomes equal to the volume of the Eulerian mesh Δx^3, where the Lagrangian grid volume is defined by assuming a particle as a shell with thickness Δx. A virtual solid wall is used to model the pipe geometry in a rectangular computational domain. This is implemented by means of a volume penalization technique that is explained in the next subsection.

Accounting for the inertia of the fictitious fluid phase inside the particle volume, Breugem (2012) showed that Eqs. (3) and (4) can be rewritten as:

$$\rho_p V_p \frac{dU_p}{dt} \approx -\rho_f \sum_{l=1}^{N_L} F_l \Delta V_l + \rho_f \frac{d}{dt}\left(\int_{V_p} u dV\right) + F_c, \quad (7)$$

$$\frac{d(I_p \omega_p)}{dt} \approx -\rho_f \sum_{l=1}^{N_L} r_l \times F_l \Delta V_l + \rho_f \frac{d}{dt}\left(\int_{V_p} r \times u dV\right) + T_c. \quad (8)$$

The point force F_l is calculated at each Lagrangian point using the difference between the particle surface velocity ($U_p + \omega_p \times r$) and the interpolated first prediction velocity at the same point. The first prediction velocity is obtained by advancing Eq. (1) in time without considering the force field f.

The forces, F_l, integrate to the force field f using the regularized Dirac delta function δ_d of Roma et al. (1999):

$$f_{ijk} = \sum_{l=1}^{N_L} F_l \delta_d(x_{ijk} - X_l)\Delta V_l \quad (9)$$

with x_{ijk} and X_l referring to an Eulerian and a Lagrangian grid cell. This smooth delta function essentially replaces the sharp interface with a thin porous shell of width $3\Delta x$; it preserves the total force and torque on the particle provided that the Eulerian grid is uniform. An iterative algorithm is employed to calculate the force field f, allowing for a better estimate of no-slip and no-penetration boundary conditions Breugem (2012). A lubrication correction based on the asymptotic analytical expression for the normal lubrication Jeffrey (1982) is used when the distance between particles (or a particle and a wall) is smaller than one Eulerian grid size and a soft-sphere collision model with Coulomb friction takes over the interaction when the particles touch. These short-range interaction forces and torques are represented in the equations 7–(8) by F_c and T_c, respectively. More details about the models and validations can be found in Ardekani et al. (2016); Costa et al. (2015).

Using the volume of fluid (VoF) approach, proposed in Ardekani et al. (2018), the velocity of the combined phase is defined at each point in the domain as

$$u_{cp} = (1 - \xi)u_f + \xi u_p, \quad (10)$$

where u_f is the fluid velocity and u_p the solid phase velocity, obtained by the rigid body motion of the particle at the desired point. In other words, the fictitious velocity of the fluid phase trapped inside the particles is replaced by the particle rigid body motion velocity when solving the temperature equation inside the solid phase; this velocity is computed as $U_p + \omega_p \times R$ with R, the position vector from the center of the particle. ξ is a phase indicator, obtained from the location of the fluid/solid interface exactly for rigid spheres and used to distinguish the solid and the fluid phase within the computational domain. ξ is computed at the velocity (cell faces) and the pressure points (cell center) throughout the staggered Eulerian grid. This value varies between 0 and 1 based on the solid volume fraction of a cell of size Δx around the desired point. u_{cp} is then used in Eq. (6) where the same thermal diffusivity in both phases is considered. It should be noted that the computed u_{cp} remains a divergence free velocity field.

Spatial derivatives are estimated with the central-differencing scheme, except for the term $u_{cp} \cdot \nabla T$, where an explicit fifth-order WENO scheme Liu et al. (1994) is used to avoid dispersive behaviours of the temperature field. Thermal diffusion terms are computed continuously, both inside and outside of the particles, using central difference with the same thermal diffusivity for the particles and the fluid. The governing equations for the fluid phase, particles motion and temperature are integrated in time using an explicit low-storage Runge–Kutta method Wesseling (2009) with the pressure-correction scheme used in Breugem (2012) to project the velocity field onto the divergence-free space.

2.3. Flow geometry

A volume penalization method is employed to create a cylindrical pipe inside a rectangular numerical domain with uniform Cartesian grids. Kajishima et al. (2001) and Breugem et al. (2014) proposed the volume penalization IBM, where the IBM force f is calculated from the prediction velocity and the local solid volume fraction. In this study we initially compute the first prediction velocity u^* by integrating Eq. (1) in time without considering the IBM force and the pressure correction. Next, the IBM induced by the particles (this step is given in the previous section), is added to u^* to create the second prediction velocity u^{**}. Finally, the volume penalization IBM force f and the third prediction velocity u^{***} are calculated as follows:

$$f_{ijk} = \mathscr{S}_{ijk} \frac{(u_s - u^{**})_{ijk}}{\Delta t}, \quad (11a)$$

$$u_{ijk}^{***} = u_{ijk}^{**} + \Delta t f_{ijk}, \quad (11b)$$

where $\mathscr{S}_{ijk}$ is the solid volume fraction in the grid cell with index (i, j, k), varying between 0 (entirely located in the fluid phase) and 1 (entirely located in the solid area) and u_s is the solid interface velocity within this grid cell. Fig. 1 indicates the solid volume fractions (highlighted area) for grid cells around $u(i, j)$ and $v(i - 1, j - 1)$. The solid boundary in this figure is shown by the red dashed line. For non-moving boundaries, u_s is 0 and Eq. (11) reduce to:

$$u_{ijk}^{***} = (1 - \mathscr{S}_{ijk})u_{ijk}^{**}. \quad (12)$$

The third prediction velocity is then used to update velocities and pressure following a classical pressure correction scheme (Breugem, 2012). The volume penalization IBM is computationally efficient since the solid volume fractions around velocity points can be calculated at the beginning of the simulation with an accurate method and it allows the use of FFT based pressure equation solvers. To validate the employed volume penalization technique, we plot the mean fluid velocity of the single-phase turbulent
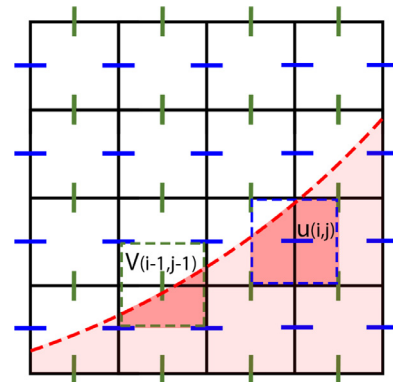

Fig. 1. Solid volume fractions (highlighted area) for grid cells around $u(i, j)$ and $v(i - 1, j - 1)$. Solid boundary is shown by red dashed line.
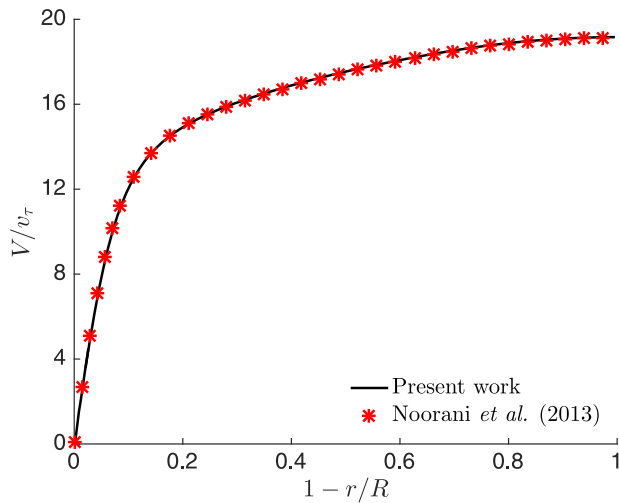
Fig. 2. The mean velocity profile for $Re_b = 5300$, normalized by the friction velocity v_τ, compared to the study by Noorani et al. (2013).

flow with $Re_b = 5300$, against the results in Noorani et al. (2013) obtained with the spectral code nek5000 Fischer et al. (2008). Fig. 2 indicates a perfect match between the two mean velocity profiles. This simulation is performed with an uniform Cartesian mesh of $7200 \times 600 \times 600$ grid points in the x (streamwise), y and z directions, corresponding to a grid spacing of approximately 0.6^+ in wall units. In addition to the 600 grid points defining the diameter of the pipe, few extra points are considered in the cross-stream section to optimize the performance of the FFT based pressure solver.

Here, we investigate the effect of particle size and volume fraction on the heat transfer through suspensions of neutrally buoyant, rigid, spherical particles. For this purpose, we perform direct numerical simulations (DNS) of particle suspensions on a Cartesian grid where a cylindrical pipe is created by means of the volume penalization IBM introduced above. Heat transfer in laminar suspensions is studied for different particle volume fractions and different pipe to particle diameter ratios, while for the turbulent regime the effect of volume fraction is investigated for one particle size. Details of the parameters used in the simulations are given in Table 1. Periodic boundary conditions are used for both velocity and temperature in the streamwise direction, while a constant surface temperature T_s is considered at the pipe walls. The simulations are initialised with an already fully developed flow with zero temperature both inside and outside the particles. The flow statistics are collected for sufficiently long times and averages computed in time, streamwise and azimuthal directions in the solid and fluid phases, while the transient behaviour is studied for the temperature fields.

Table 1

Parameters defining the different cases studied. D/d indicates the pipe to particle diameter ratio, L is the pipe length, Re_b is the bulk Reynolds number of the suspension, defined by means of the pipe diameter D and the bulk velocity V_b, Pr is the Prandtl number, ϕ the solid volume fraction. The resolution pertains the size of the Eulerian mesh and N_l the number of Lagrangian points on the surface of each individual particle. The particles are assumed to have the same density and thermal diffusivity of the fluid. The grid spacing in the turbulent cases is approximately 0.6^+ in wall units of the single-phase flow case.

D/d	L	Re_b	Pr	ϕ	Resolution	N_l
5	$4D$	370	7	0,5,15,30 & 40%	$640 \times 160 \times 160 \,(32/d)$	3220
10	$4D$	370	7	0,5,15,30 & 40%	$1280 \times 320 \times 320 \,(32/d)$	3220
15	$4D$	370	7	0,5,15,30 & 40%	$1920 \times 480 \times 480 \,(32/d)$	3220
15	$12D$	5300	7	0,5,15,30 & 40%	$7200 \times 600 \times 600 \,(40/d)$	5035

3. Results

3.1. Laminar regime

The results pertaining the heat transfer in laminar flows are reported in this section. Firstly, the mean velocity profiles are depicted in Fig. 3 for different volume fractions and different particle sizes. It can be observed that the profile tends to be more uniform as the volume fraction increases or as the pipe to particle diameter ratio, D/d, decreases. More uniform profiles are generated as a consequence of a momentum exchange in the radial direction by means of fluid and particle velocity fluctuations, as well as particle stresses, whereas in laminar single-phase flows momentum is only transferred by molecular diffusion. The total drag associated to the laminar flows will be discussed below when displaying the suspension effective viscosity.

We now move to quantify the heat transfer enhancement in the radial direction for laminar cases. Assuming a long periodic cylinder of radius R initially at $T = 0$ with constant surface temperature of T_s, the heat equation can be simplified to pure conduction as below:

$$\frac{1}{\alpha}\frac{dT}{dt} = \frac{1}{r}\frac{d}{dr}\left(r\frac{dT}{dr}\right),$$

(13)

with α, the thermal diffusivity of the fluid. Noting this is an eigenvalue problem, one can assume a solution of the form $T(r, t) = \Phi(r)\Gamma(t)$ and obtain an analytical solution Incropera et al. (2007) in the form

$$T(r, t) = T_s - \frac{2}{R}\sum_{n=1}^{\infty}\frac{J_0(\lambda_n r)}{\lambda_n J_1(\lambda_n R)}exp(-\alpha\lambda_n^2 t),$$

(14)

where J_0 and J_1 are the Bessel functions of first kind of order zero and one, respectively, and λ_n the eigenvalues, given as the roots of $J_0(\lambda R) = 0$. The first four eigenvalues are $\lambda_1 = 2.405/R$, $\lambda_2 = 5.520/R$, $\lambda_3 = 8.654/R$ and $\lambda_4 = 11.79/R$. It can be shown that the mean temperature can be expressed exploiting the series above by averaging the equation with respect to r.

An effective thermal diffusivity for the laminar suspension can therefore be defined by assuming a solution of the form above and evaluating the time history of the mean temperature inside the pipe. The mean temperature T_m converges exponentially to the surface temperature T_s, after a sufficiently long time when λ_1 becomes the dominant term in the solution series. The effective thermal diffusivity of the suspension α_e is then calculated as:

$$\alpha_e \equiv -\frac{d\ln\left[1 - \frac{T_m(t)}{T_s}\right]}{\lambda_1^2 \, dt^*}\Bigg|_{t\gg 1},$$

(15)

where the non-dimensional time $t^* = tV_b/D$. For a better understanding of the procedure above, the time histories of $-\ln[1 - T_m/T_s]/\lambda_1^2$ are reported in Fig. 4 for suspension of particles of size $D/d = 5$ with different volume fractions together with their linear fits, indicated by black dotted lines. The slopes of these linear fits then define the effective thermal diffusivities. This quantity will be used in the following to quantify the effect of the solid suspended phase on the heat transfer process.

The effective thermal diffusivity of the suspension, extracted from our simulations and normalized by that of the fluid is depicted in figure 5(a) for the laminar cases under investigation here. This ratio, α_r, is considered as a measure for heat transfer enhancement. The data in the figure show a significant increase in α_r as the particle volume fraction increases. Interestingly, a saturation can be observed for small particles when the volume fraction exceeds 30%. A significant reduction in the heat transfer enhancement is observed as D/d increases, which can be associated to a reduction of inertial effects at the particle scale Ardekani et al. (2018). In fact, Metzger et al. (2013) reported a linear increase of heat transfer with volume fraction for low particle Reynolds numbers ($Re_p < 0.5$) in a Couette flow and a saturation of this
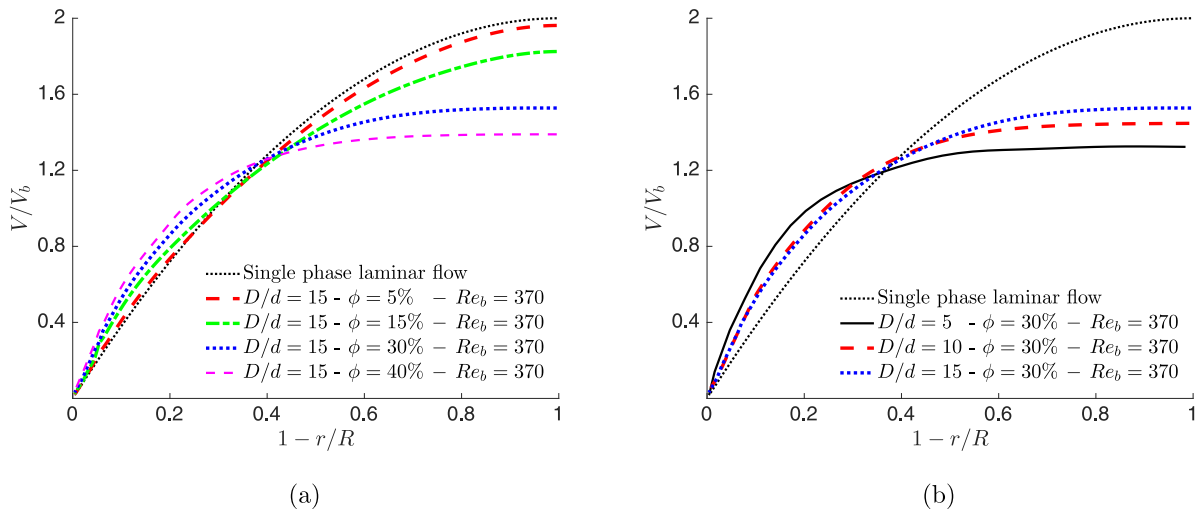
Fig. 3. Mean velocity profiles, normalized by the bulk velocity, depicted for (*a*) different volume fractions at $D/d = 15$ and (*b*) different pipe to particle diameter ratios. The mean velocity profile for a laminar pipe flow is indicated by a black dotted line as reference.
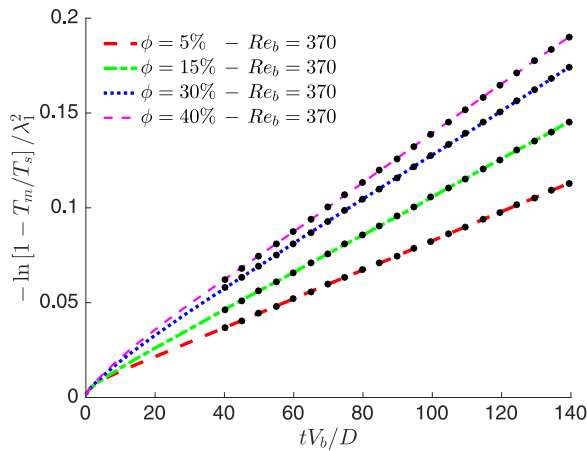

Fig. 4. $-\ln[1 - T_m/T_s]/\lambda_1^2$ versus non-dimensional time, tV_b/D, for suspension of particles of size $D/d = 5$ with different volume fractions. The effective thermal diffusivities are calculated from the slopes of the linear fits, indicated by the black dotted lines.
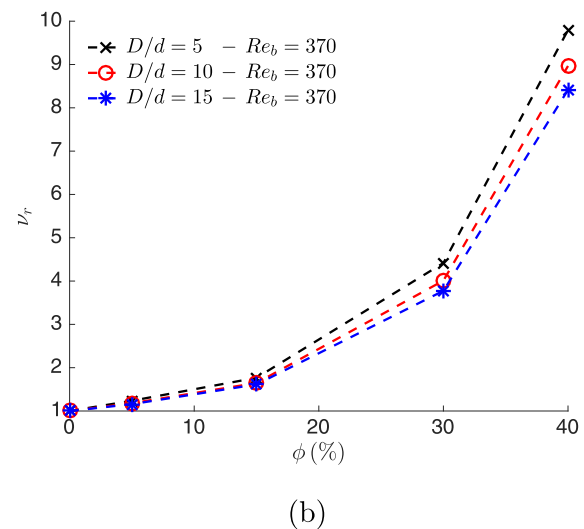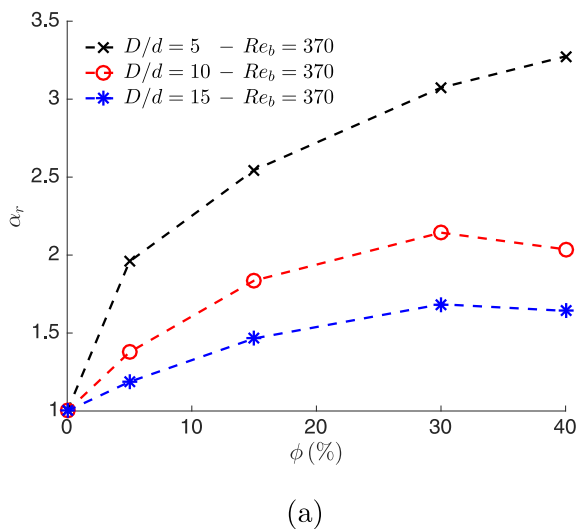
linear increase at about $\phi = 40\%$. The effect of particle inertia has been shown in Ardekani et al. (2018) to increase heat transfer beyond the linear trend reported in Stokes flow, more clearly for values $Re_p > 4$. The particle Reynolds number, Re_p, can be approximately defined as $Re_b/(D/d)^2$ for the pressure driven flows examined in this work. In this case, the smallest Re_p is attained for particles with $D/d = 15$, when $Re_p = 1.64$, so that inertial effects are not negligible for the cases considered here.

The effective viscosity of the suspension, normalized by the viscosity of the fluid is given in Fig. 5(*b*). The effective viscosity is defined as the viscosity that produces the same amount of drag on the pipe walls in single-phase laminar flow; in other words, the ratio ν_r in Fig. 5(*b*) indicates the wall-drag increase in the presence of particles. Interestingly, it can be observed that while the heat transfer is enhanced significantly when using larger particles, the effect of the particle size on the wall-drag is less pronounced. The effective viscosity of the suspension is mainly determined by excluded volume effects, the nominal particle volume fraction, and the particle size has a secondary role on the total viscous dissipation in laminar flows for the cases considered here. As regards heat transfer, thermal diffusion is relatively weaker than viscous diffusion as the Prandtl number $Pr = 7$, and thus the fluid
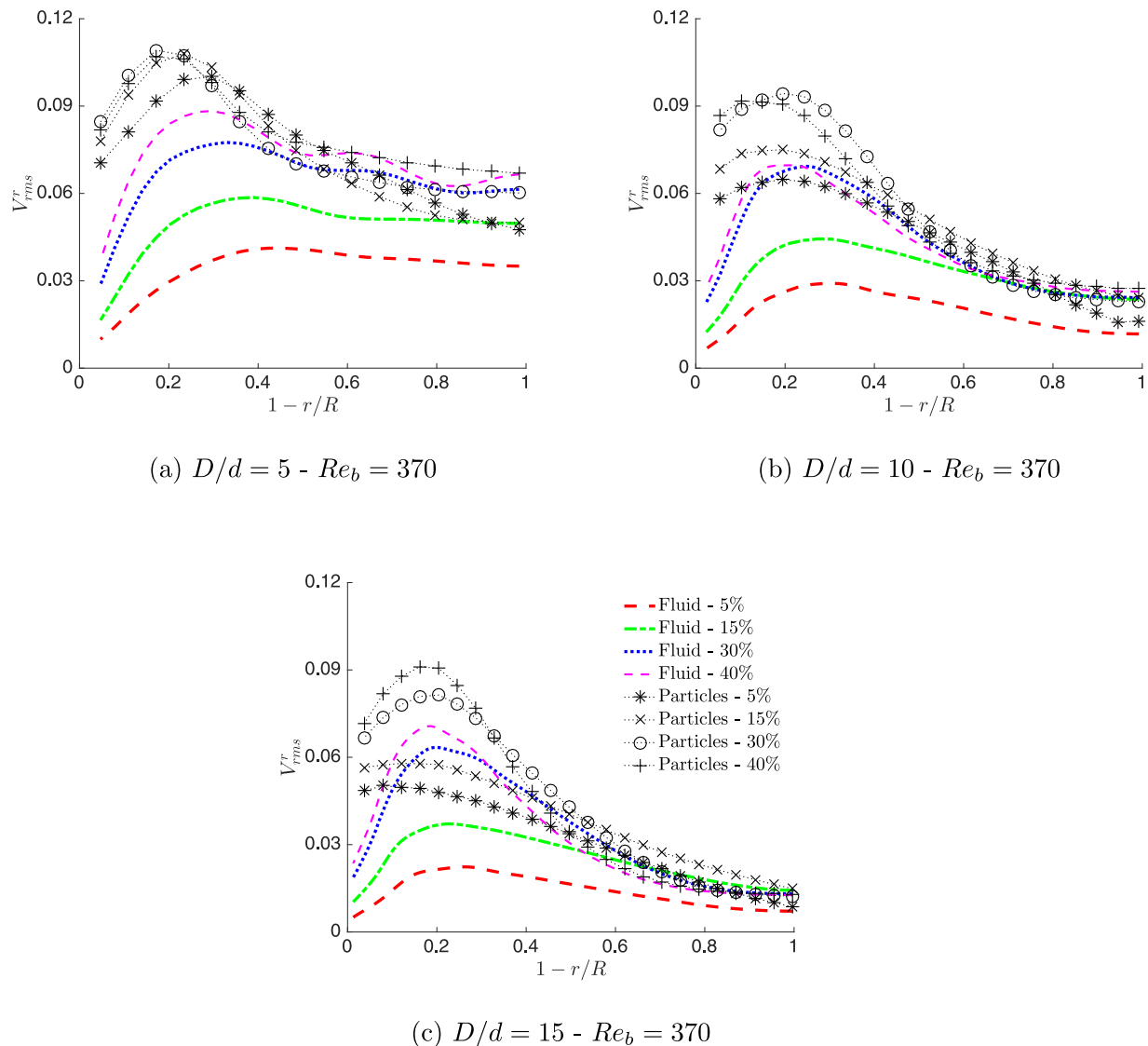

Fig. 5. The effective thermal diffusivity, (*a*) and the effective viscosity (*b*) of the suspension for different volume fractions and different pipe to particle diameter ratios, normalized by the thermal diffusivity and viscosity of the fluid respectively.

(a) $D/d = 5$ - $Re_b = 370$

(b) $D/d = 10$ - $Re_b = 370$

(c) $D/d = 15$ - $Re_b = 370$

Fig. 6. R.M.S of the radial velocity fluctuations, normalized by the bulk velocity V_b, versus the distance from the pipe wall for different particle sizes. $(a) D/d = 5$, $(b) D/d = 10$ and $(c) D/d = 15$.

and particle velocity fluctuations play a more prominent role in the heat transfer, also because particles do not directly affect heat transfer by their only presence as they do for the momentum. Since increasing the particle size increases the velocity fluctuations and thus prominently the heat transfer, we find the the effective thermal diffusivity to vary more with the particle size. The ratio between α_r and ν_r can be seen as the heat transfer enhancement achieved by means of suspended particles divided by the cost of pumping a more viscous fluid and can be seen as a relevant design variable. Our results indicate that using large particles is more effective in this regards.

Ardekani et al. (2018) showed that when the particle Reynolds number is large enough the fraction of heat transfer conducted inside the particles is negligible and the velocity fluctuations of both fluid and particles are the main mechanisms for heat transfer. We therefore display the radial distributions of the radial velocity fluctuations for the fluid and particle phases in Fig. 6, again for different particle sizes and volume fractions. The plots reveal that the velocity fluctuation profiles have a peak near the wall and then rapidly decay in the core region in the presence of small particles, while for large particles ($D/d = 5$) the velocity fluctuations remain high throughout the pipe cross-section. Another interesting observation is the saturation of the fluid velocity fluctuations for volume fractions above $\phi = 30\%$, which is again not

observed for large particles. This behaviour explains the absence of a saturation in the heat transfer enhancement above $\phi = 30\%$ for the largest particles studied here (see Fig. 5(a)). The particle velocity fluctuations are observed to be larger than that of the fluid, so that these can be seen as the cause of the fluid velocity fluctuations. Particles effectively transfer heat across the pipe, acting as mobile energy sources that bring high temperature from the wall-region to the center of the pipe.

The particle rotation close to the wall region, note the highest temperature is imposed at the walls, disrupts the thermal boundary layer forming by conduction at the wall, lifting hot fluid towards the pipe core. These rotation rates are thus depicted in figure 7 and compared for different volume fractions and particle sizes. It is observed that close to the wall the particle rotation rate increases with volume fraction while it decreases in the pipe core region. A significant increase in the rotation rates is observed throughout the pipe when the particles size relative to the pipe diameter increases. The fluid around inertial particles is centrifuged by the particle rotation, bringing hot fluid to the cold region in the pipe center. This observation is consistent with the experiments of Ahuja (1975), who suggested a similar mechanism for the heat transfer enhancement in the presence of inertial particles ($Re_p > 1$).
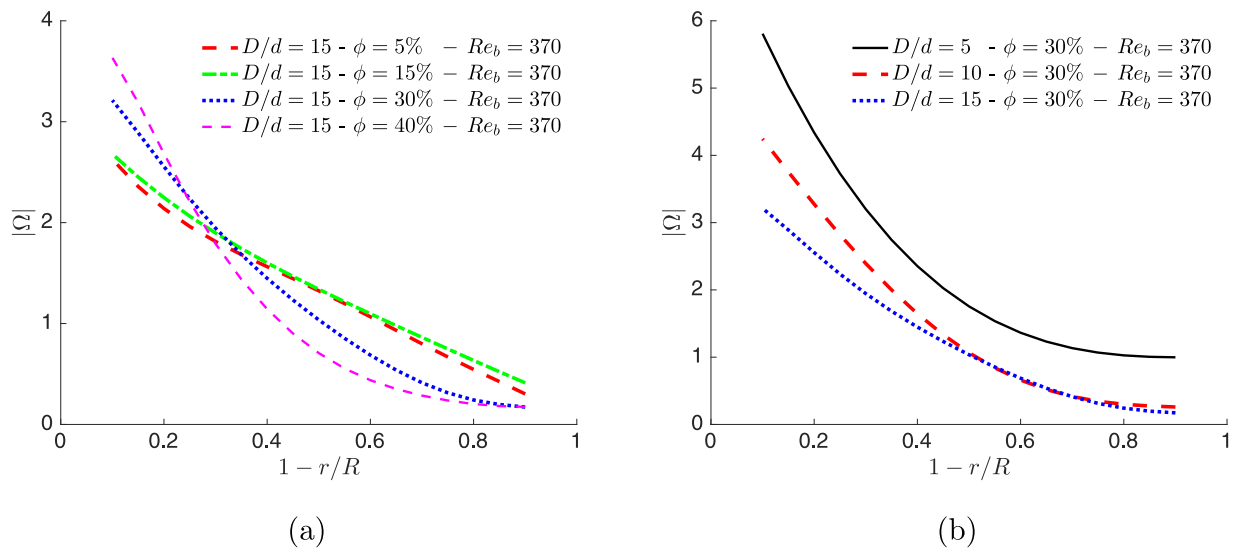
Fig. 7. Rotation rate of the particles, normalized by V_b/D for (a) various volume fractions with $D/d = 15$ and (b) different particle sizes at $\phi = 30\%$.
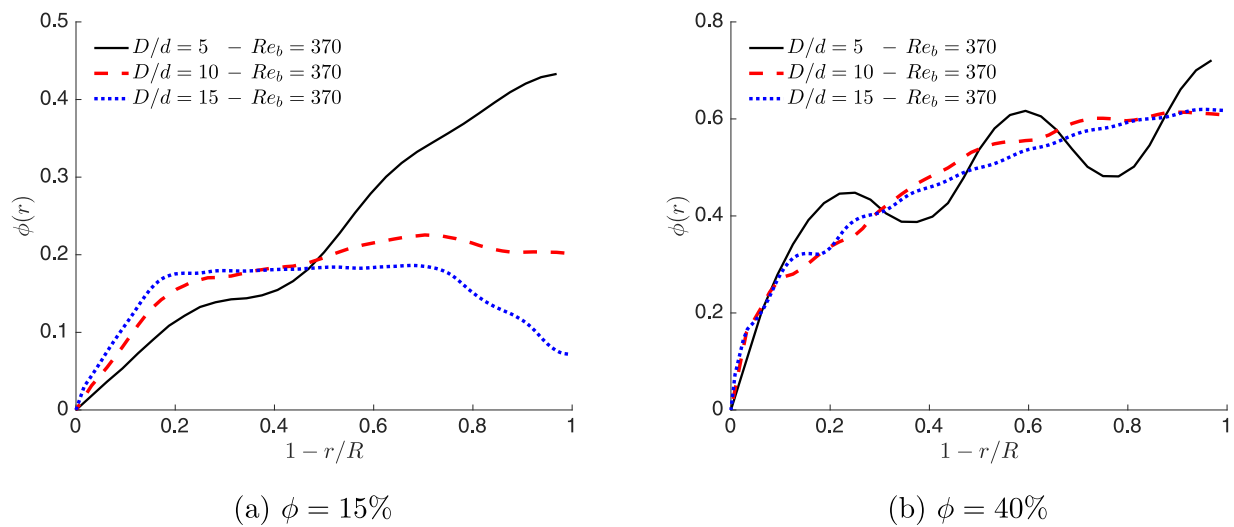

Fig. 8. Radial particle concentration profiles for different pipe to particle diameter ratios at different volume fractions. (a) $\phi = 15\%$ and (b) $\phi = 40\%$.

The larger rotation rates experienced by larger particles close to the wall create flow structures able to bring fluid particles into the core region; on other hand, larger particles experience larger lift forces towards the center of the pipe according to the findings of Hood et al. (2015) and Lashgari et al. (2017) on inertial migration of spherical particles in laminar square duct flows. This size effect can be observed in Fig. 8, where we report the radial mean particle concentration for different size ratios at volume fraction $\phi = 15$ and 40%. For lower volume fractions (see Fig. 8(a)), when the particles have more freedom to move in the radial direction, the largest particles are observed to migrate towards the center of the pipe while the opposite holds as the particle size decreases. When the volume fraction increases, particles have less freedom to migrate and preferentially accumulate and instead form layers. These layers can be observed in Fig. 8(b), where the concentration profiles at high volume fraction, $\phi = 40\%$, are depicted. Particles move from one layer to the other occasionally, increasing the mixing inside the pipe. It should be noted this heat-transfer mechanism is more relevant when the particle size is considerable compared to the pipe diameter, i.e. when changing layer can transfer heat by a greater distance.

3.2. Turbulent regime

Statistics pertaining the turbulent flow and the associated heat transfer are reported in this section. The mean velocity profiles for the fluid and particle phase are shown in Fig. 9(a). The center line velocity is observed to increase with the volume fraction, reaching to its maximum at $\phi = 15\%$ and then decreasing to a value below that of the single phase flow at $\phi = 40\%$. The mean streamwise particle velocity, depicted in this figure with black dots, perfectly matches the mean velocity of the fluid except for a small region close to the wall where a deviation can be observed. This is due to the no-slip boundary condition for the fluid phase, which does not hold for the particles.

The particle concentration profiles are reported in Fig. 9(b) for the different volume fractions under investigations. The concentration peak close to the wall increases with the volume fraction of the suspension. This is consistent with the findings of Costa et al. (2016), who showed that a layer of particles forms near the wall in turbulent channel flows laden with finite-size spherical particles; this wall layer is associated to an increase of the turbulent drag. The friction Reynolds number Re_τ is depicted in Fig. 10(a) versus the volume fraction ϕ. The drag, expressed in terms of Re_τ, increases first gradually at low volume fractions and
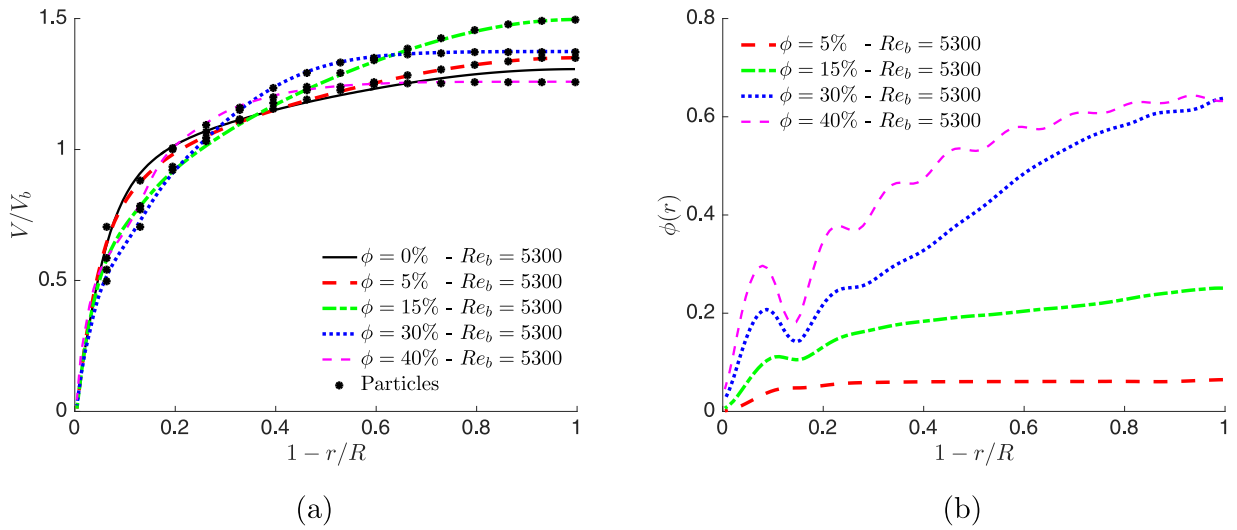
Fig. 9. Radial profiles of (*a*) the mean stremwise fluid velocity and (*b*) particle concentration. The mean particle velocity is indicated in panel (*a*) with dots.

then more rapidly $\phi > 15\%$.

Quantifying the heat transfer in the turbulent cases cannot be done as previously in the laminar regime due to the strong variation of the effective thermal diffusivity in time; we therefore resort to a different approach to document the effect of the suspended phase on the heating of the flow in the pipe when fixing the wall temperature, see also Incropera et al. (2007). We describe the mean temperature growth in the periodic numerical domain by means of an effective equation,

$$mC_p \frac{dT_m}{dt} = q^{''}A \equiv h(T_s - T_m)A ,$$

(16)

where m is the mass of the suspension, q'' is the heat flux, A indicates the surface area of the pipe and h is the local convection heat transfer coefficient. Introducing the new variable $\Delta T \equiv T_s - T_m$, Eq. (16) can be rewritten in the following form:

$$\frac{d\Delta T}{dt} = -\frac{4}{\rho C_p D}h\Delta T ,$$

(17)

which is integrated in time from zero to yield

$$\ln\left(\frac{\Delta T}{\Delta T_0}\right) = -\frac{4t}{\rho C_p D}\left(\frac{1}{t}\int_0^t h\,dt\right) \equiv -\frac{4t}{\rho C_p D}\bar{h} .$$

(18)

An average convection heat transfer coefficient $\bar{h}$ is defined as the time average of the local convection coefficient, where the average is taken from time zero. Rewriting Eq. (18) in non-dimensional form and given at $t = 0$, $\Delta T_0 = T_s$, the following expression is derived to describe the transient heat transfer:

$$\overline{Nu}(t^*) = -\frac{1}{4t^*}RePr \ln\left[1 - \frac{T_m(t)}{T_s}\right],$$

(19)

where, $\overline{Nu} \equiv \bar{h}D/k$ is the Nusselt number, averaged from time zero and t^* is the non-dimensional time in units of D/V_b. This can be seen as the temporal counterpart of the Nusselt number defined for spatially developing heating problems Incropera et al. (2007).

The Nusselt number, $\overline{Nu}$, is the ratio of convective to conductive heat transfer from the surface of the pipe. This quantity is depicted in time for different solid volume fractions in Fig. 10(b). A significant heat transfer enhancement is observed initially with increasing the volume fraction ($t^* \lesssim 100$); however, $\overline{Nu}$ decays in time for the flows with high volume fractions, even to values below those for the single phase flow. An overall increase in the heat transfer, with respect to the single phase flow, is found for long times ($t^* > 150$) only for the case at low volume fraction $\phi = 5\%$.

To understand this behaviour, the different components of the fluid velocity fluctuations and the Reynolds shear stress profiles are displayed in Fig. 11(a) –(d). The streamwise velocity fluctuations increase at $\phi = 5\%$ and significantly decrease for the cases with high volume fraction, $\phi = 30$ and 40%. At $\phi = 15\%$, however, the near-wall fluctuation peak is dampened while the fluctuations increase in the core region of the pipe. The radial velocity fluctuations are observed to grow with the volume fraction in the vicinity of the pipe wall, and to decay in the core region when ϕ increases, except for $\phi = 5\%$ where the radial velocity fluctuations increase throughout the whole pipe cross-section. Interestingly, the velocity fluctuations are significantly attenuated in all
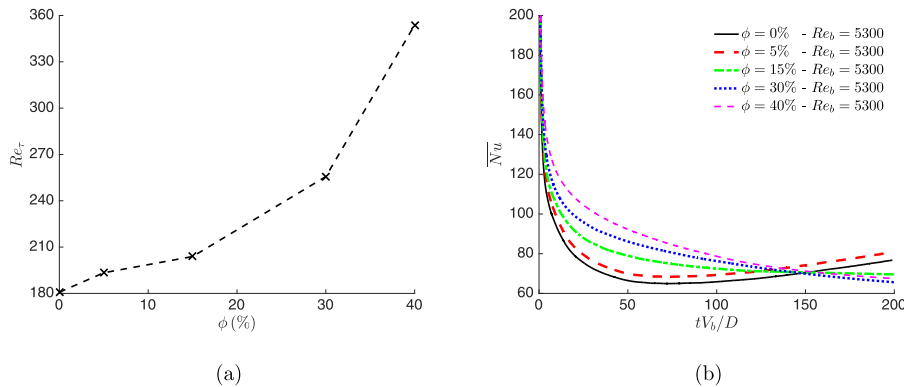

Fig. 10. (*a*): The friction Reynolds number Re_τ versus the volume fraction ϕ and (*b*): the time variation of the Nusselt number, $\overline{Nu}$, a value representing the average heat flux from time zero for each of the different volume fractions considered.
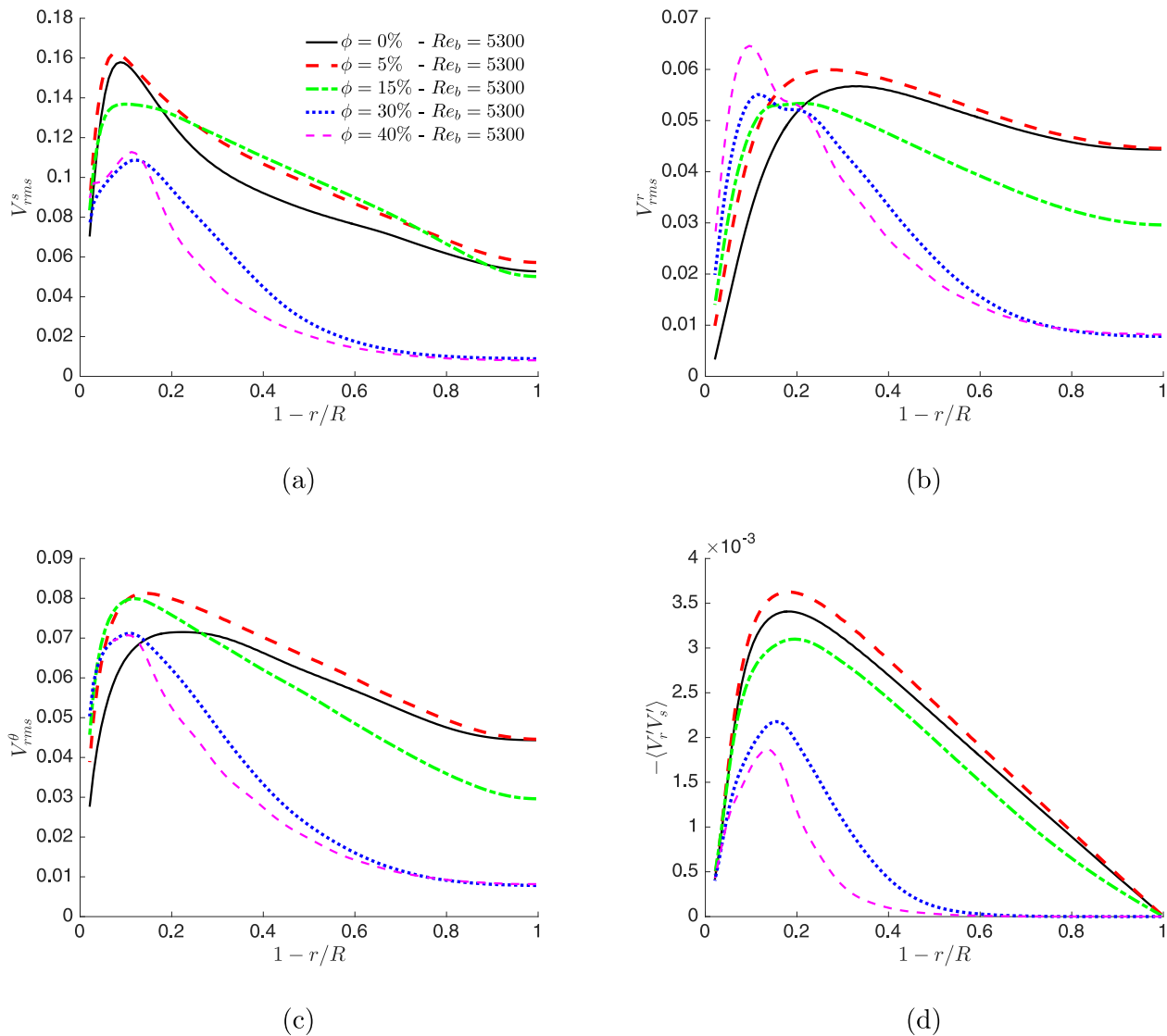
Fig. 11. R.M.S of fluid velocity fluctuations, normalized by the bulk velocity, for the different volume fractions under investigation versus the distance from the wall. (*a*) streamwise, (*b*) radial and (*c*) azimuthal component. The Reynolds shear stress profiles are depicted in panel (*d*).

directions in the pipe center for the cases with high volume fractions, $\phi = 30$ and 40%. In fact, the suspension is laminarized in the core region for these cases as shown by the fact that the Reynolds shear stress tends to zero in this region. These high volume fraction cases are in the inertial shear-thickening regime, where the particle induce stress are the main mechanism for momentum transfer. This is consistent with the findings of Lashgari et al. (2014) in particulate channel flows, where they document the existence of three different regimes by changing the volume fraction ϕ and the bulk Reynolds number Re_b. For lower volume fractions, a turbulence attenuation is observed at $\phi = 15$%, while enhancement of the turbulence activity, measured with respect to the single phase flow, can be seen at $\phi = 5$%.

We therefore attribute the initial heat transfer enhancement observed at high volume fractions to the increase of the radial velocity fluctuations close to the wall. However, due to the quenching of turbulence in the pipe core, conduction takes over as dominant heat transfer mechanism. This causes a strong decay in the heat transfer process, which is hence is less effective towards the pipe center. To confirm this, we display in Fig. 12 contours of the fluid and particle temperature in one of the pipe cross sections. The heat transfer process is compared between the two cases at $\phi = 5$% and $\phi = 40$%. The visualisation reveals that mixing is significantly delayed at $\phi = 40$%.

Initially, the larger velocity fluctuations close to the wall observed in the case with $\phi = 40$% effectively accelerate the heat transfer from the pipe wall, as demonstrated by the higher mean temperature in Fig. 12(d) and (e), when compared to 12(a) and (b), respectively. However the hot fluid close to the wall cannot be easily convected to the centreline when the flow is laminar-like at high particle volume fractions, which decelerate the heat transfer process. T_m is therefore higher in Fig. 12(c) than in 12(f).

4. Final remarks

We report results from particle-resolved direct numerical simulations (PR-DNS) of heat transfer in laminar and turbulent pipe flows laden with neutrally buoyant, rigid, spherical particles. We assume the pipe walls at fixed temperature and examine the time evolution of the temperature of the fluid and particles inside the pipe. In this study, we focus on the effect of particle size and volume fraction on the heat transfer process. Various particle volume fractions, up to $\phi = 40$%, and different pipe to particle diameter ratios are considered in laminar suspensions, while for the turbulent regime, also owing to the increased computational cost, the effect of volume fraction is investigated. We perform simulations of particle suspension on a Cartesian grid where a
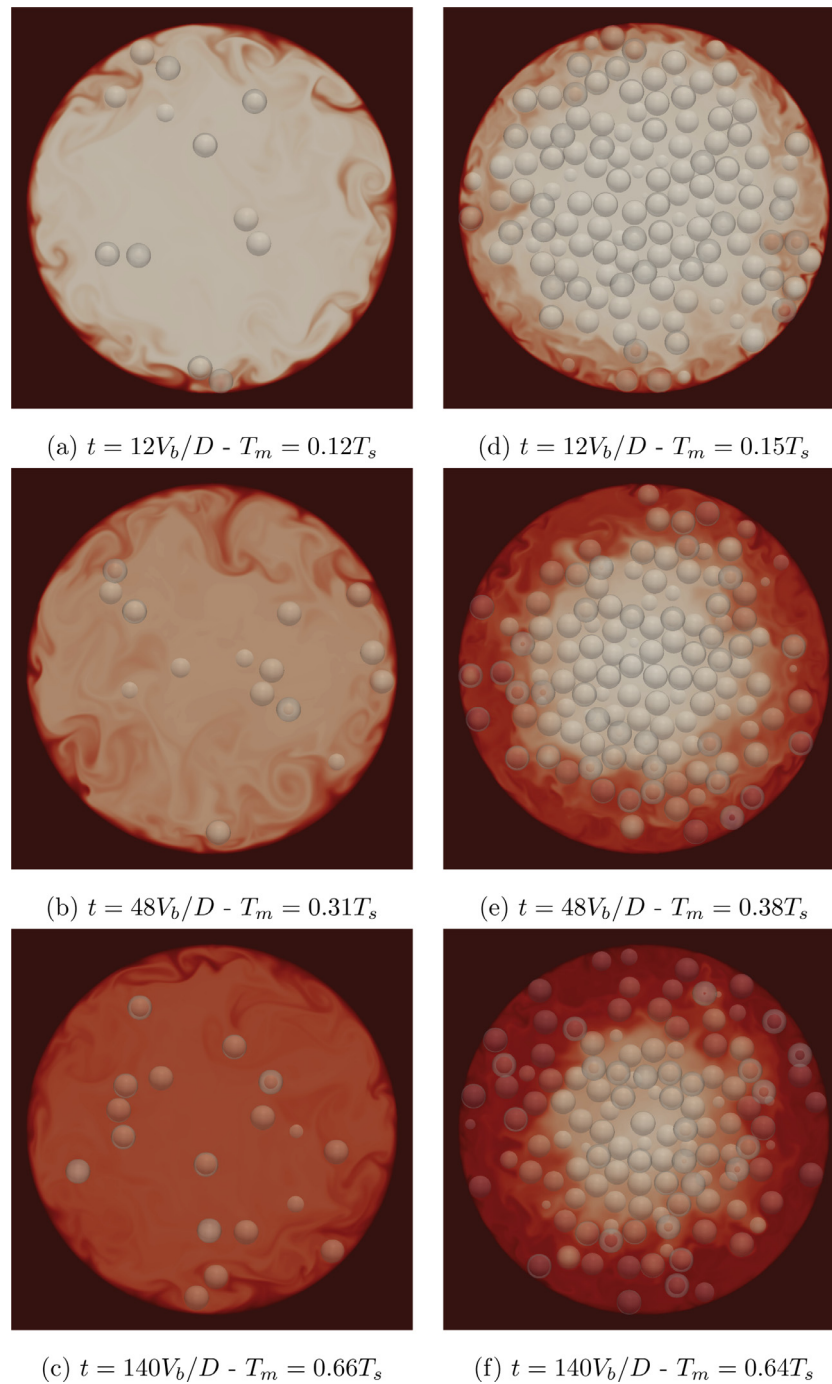
(a) $t = 12V_b/D$ - $T_m = 0.12T_s$

(d) $t = 12V_b/D$ - $T_m = 0.15T_s$

(b) $t = 48V_b/D$ - $T_m = 0.31T_s$

(e) $t = 48V_b/D$ - $T_m = 0.38T_s$

(c) $t = 140V_b/D$ - $T_m = 0.66T_s$

(f) $t = 140V_b/D$ - $T_m = 0.64T_s$

Fig. 12. Instantaneous contours of temperature inside the pipe for $(a − c)$ $\phi = 5\%$ and $(d − f)$ $\phi = 40\%$, $Re_b = 5300$.

cylindrical pipe is created by means of volume penalization IBM. The numerical algorithm is based on an immersed boundary method (IBM) to resolve fluid-solid interactions with lubrication and contact models for the short-range particle-particle (particle-wall) interactions. A volume of fluid (VoF) model is used to solve the heat transfer equation both inside and outside of the particles.

We show that a considerable heat transfer enhancement (up to 330%) can be achieved in the laminar regime by adding spherical particles. For the parameter range investigated here, the heat transfer is observed to increase significantly as the pipe to particle diameter ratio decreases. Larger particles are shown to have a greater impact on the heat transfer enhancement than on the wall-drag increase, indeed the suspension effective viscosity is found to be almost independent of the

particle size and mainly depend on the solid volume fraction. In addition the saturation of the heat transfer enhancement that is observed for smaller particles, $D/d = 10$ and 15, when the particle volume fraction exceeds $\phi = 30\%$, is not found for the larger particles ($D/d = 5$). In this case, the heat transfer continuously increase up to $\phi = 40\%$, the largest value considered here.

We also document a significant increase of the particle rotation rates throughout the pipe when the particle size with respect to the pipe diameter increases. The fluid around inertial particles is centrifuged by the particle rotation, bringing hot fluid from the wall region to the colder pipe core. The largest particles, studied here, are observed to migrate towards the center of the pipe, acting effectively as energy conveyor and enhancing the heat transfer from the pipe wall.

In the turbulent regime, we study the transient heating induced by the hot pipe walls. A significant heat transfer enhancement is observed at early times when increasing the volume fraction. However, the average Nusselt number, $\overline{Nu}$, decays in time to values below the single phase case for the flows with high particle volume fractions. An overall increase in the heat transfer, with respect to the single phase flow, is reported only for the case with lowest volume fraction, $\phi = 5\%$. To explain this behaviour we show that the radial velocity turbulent fluctuations increase with the solid volume fraction in the vicinity of the pipe wall, whereas the overall turbulent activity reduces in the core region when ϕ increases above 10%. The suspension is re-laminarized in the core region for high particle volume fractions, $\phi = 30$ and 40%, which slows down significantly the heat transfer towards the centreline. In other words, the larger radial velocity fluctuations in the near-wall region accelerate the heat transfer from the pipe wall at early times, while the turbulence attenuation decelerate the later stages of the heating process, those pertaining the pipe core. At $\phi = 5\%$, conversely, the radial velocity fluctuations are increased all over the pipe, which explains why this is the optimal case among those considered here. Future efforts may focus on optimising the effects of the dispersed phase on the heat transfer, considering also non-spherical particles and different thermal properties of the solid phase.

Acknowledgments

References

Ahuja, A.S., 1975. Augmentation of heat transport in laminar flow of polystyrene suspensions. i. experiments and results. J. Appl. Phys. 46 (8), 3408–3416.

Ardekani, M.N., Abouali, O., Picano, F., Brandt, L., 2018. Heat transfer in laminar couette flow laden with rigid spherical particles. J. Fluid Mech. 834, 308–334.

Ardekani, M.N., Costa, P., Breugem, W.P., Brandt, L., 2016. Numerical study of the sedimentation of spheroidal particles. Int. J. Multiphase Flow 87, 16–34.

Ardekani, M.N., Costa, P., Breugem, W.P., Picano, F., Brandt, L., 2017. Drag reduction in turbulent channel flow laden with finite-size oblate spheroids. J. Fluid Mech. 816, 43–70.

Avila, R., Cervantes, J., 1995. Analysis of the heat transfer coefficient in a turbulent particle pipe flow. Int. J. Heat Mass Transf. 38 (11), 1923–1932.

Breugem, W.-P., 2012. A second-order accurate immersed boundary method for fully resolved simulations of particle-laden flows. J. Comput. Phys. 231 (13), 4469–4498.

Breugem, W.P., Van Dijk, V., Delfos, R., 2014. Flows through real porous media: x-ray computed tomography, experiments, and numerical simulations. J. Fluids Eng. 136 (4), 040902.

Brown, E., Jaeger, H.M., 2009. Dynamic jamming point for shear thickening suspensions. Phys. Rev. Lett. 103 (8), 086001.

Bu, C.-S., Liu, D.-Y., Chen, X.-P., Liang, C., Duan, Y.-F., Duan, L.-B., 2013. Modeling and coupling particle scale heat transfer with dem through heat transfer mechanisms. Numer. Heat Transf. Part A 64 (1), 56–71.

Chang, J., Yang, S., Zhang, K., 2011. A particle-to-particle heat transfer model for dense gas–solid fluidized bed of binary mixture. Chem. Eng. Res. Des. 89 (7), 894–903.

Costa, P., Boersma, B., Westerweel, J., Breugem, W.-P., 2015. Collision model for fully resolved simulations of flows laden with finite-size particles. Phys. Rev. E 92 (5), 053012.

Costa, P., Picano, F., Brandt, L., Breugem, W.-P., 2016. Universal scaling laws for dense particle suspensions in turbulent wall-bounded flows. Phys. Rev. Lett. 117 (13), 134501.

Eshghinejadfard, A., Hosseini, S.A., Thévenin, D., 2017. Fully-resolved prolate spheroids in turbulent channel flows: A lattice Boltzmann study. AIP Advances 7 (9), 095007.

Fischer, P. F., Lottes, J. W., Kerkemeier, S. G., et al., 2008. nek5000 web page, 2008. URL http.

Guazzelli, E., Morris, J.F., 2011. A Physical Introduction to Suspension Dynamics. 45 Cambridge University Press.

Guha, A., 2008. Transport and deposition of particles in turbulent and laminar flow. Annu. Rev. Fluid Mech. 40, 311–341.

Hampton, R.E., Mammoli, A.A., Graham, A.L., Tetlow, N., Altobelli, S.A., 1997. Migration of particles undergoing pressure-driven flow in a circular conduit. J. Rheol. (1978-present) 41 (3), 621–640.

Hetsroni, G., Mosyak, A., Pogrebnyak, E., 2002. Effect of coarse particles on the heat transfer in a particle-laden turbulent boundary layer. Int. J.Multiphase Flow 28 (12), 1873–1894.

Hirt, C.W., Nichols, B.D., 1981. Volume of fluid (vof) method for the dynamics of free boundaries. J. Comput. Phys. 39 (1), 201–225.

Hood, K., Lee, S., Roper, M., 2015. Inertial migration of a rigid sphere in three-dimensional poiseuille flow. J. Fluid Mech. 765, 452–479.

Incropera, F.P., Lavine, A.S., Bergman, T.L., DeWitt, D.P., 2007. Fundamentals of Heat and Mass Transfer. Wiley.

Jeffrey, D., 1982. Low-reynolds-number flow between converging spheres. J. Fluid Mech.

Kajishima, T., Takiguchi, S., Hamasaki, H., Miyake, Y., 2001. Turbulence structure of particle-laden flow in a vertical plane channel due to vortex shedding. JSME Int. J. Series B Fluids Thermal Eng. 44 (4), 526–535.

Kempe, T., Fröhlich, J., 2012. An improved immersed boundary method with direct forcing for the simulation of particle laden flows. J. Comput. Phys. 231 (9), 3663–3684.

Kuerten, J.G.M., Van der Geld, C.W.M., Geurts, B.J., 2011. Turbulence modification and heat transfer enhancement by inertial particles in turbulent channel flow. Phys. Fluids 23 (12), 123301.

Kulkarni, P.M., Morris, J.F., 2008. Suspension properties at finite Reynolds number from simulated shear flow. Phys. Fluids (1994-present) 20 (4), 040602.

Lambert, R.A., Picano, F., Breugem, W.-P., Brandt, L., 2013. Active suspensions in thin films: nutrient uptake and swimmer motion. J. Fluid Mech. 733, 528–557.

Lashgari, I., Ardekani, M.N., Banerjee, I., Russom, A., Brandt, L., 2017. Inertial migration of spherical and oblate particles in straight ducts. J. Fluid Mech. 819, 540–561.

Lashgari, I., Picano, F., Brandt, L., 2015. Transition and self-sustained turbulence in dilute suspensions of finite-size particles. Theor. Appl. Mech. Lett. 5 (3), 121–125.

Lashgari, I., Picano, F., Breugem, W.P., Brandt, L., 2014. Laminar, turbulent, and inertial shear-thickening regimes in channel flow of neutrally buoyant particle suspensions. Phys. Rev. Lett. 113 (25), 254502.

Lashgari, I., Picano, F., Breugem, W.-P., Brandt, L., 2016. Channel flow of rigid sphere suspensions: particle dynamics in the inertial regime. Int. J. Multiphase Flow 78, 12–24.

Liu, C., Tang, S., Shen, L., Dong, Y., 2017. Characteristics of turbulence transport for momentum and heat in particle-laden turbulent vertical channel flows. Acta Mechanica Sinica 1–13.

Liu, X.-D., Osher, S., Chan, T., 1994. Weighted essentially non-oscillatory schemes. J. Comput. Phys. 115, 200–213.

Loisel, V., Abbas, M., Masbernat, O., Climent, E., 2013. The effect of neutrally buoyant finite-size particles on channel flows in the laminar-turbulent transition regime. Phys. Fluids (1994-present) 25 (12), 123304.

Matas, J.P., Morris, J.F., Guazzelli, E., 2003. Transition to turbulence in particulate pipe flow. Phys. Rev. Lett. 90 (1), 014501.

Metzger, B., Rahli, O., Yin, X., 2013. Heat transfer across sheared suspensions: role of the shear-induced diffusion. J. Fluid Mech. 724, 527–552.

Namburu, P.K., Das, D.K., Tanguturi, K.M., Vajjha, R.S., 2009. Numerical study of turbulent flow and heat transfer characteristics of nanofluids considering variable properties. Int. J. Thermal Sci. 48 (2), 290–302.

Naso, A., Prosperetti, A., 2010. The interaction between a solid particle and a turbulent flow. New J. Phys. 12 (3), 033040.

Noorani, A., El Khoury, G.K., Schlatter, P., 2013. Evolution of turbulence characteristics from straight to curved pipes. Int. J. Heat Fluid Flow 41, 16–26.

Picano, F., Breugem, W.P., Brandt, L., 2015. Turbulent channel flow of dense suspensions of neutrally buoyant spheres. J. Fluid Mech. 764, 463–487.

Picano, F., Breugem, W.P., Mitra, D., Brandt, L., 2013. Shear thickening in non-brownian suspensions: an excluded volume effect. Phys.Rev. Lett. 111 (9), 098302.

Roma, A., Peskin, C., Berger, M., 1999. An adaptive version of the immersed boundary method. J. Comput. Phys. 153 (2), 509–534.

Shin, S., Lee, S.H., 2000. Thermal conductivity of suspensions in shear flow fields. Int. J. Heat Mass Transf. 43 (23), 4275–4284.

Ström, H., Sasic, S., 2013. A multiphase dns approach for handling solid particles motion with heat transfer. Int. J. Multiphase Flow 53, 75–87.

Uhlmann, M., 2005. An immersed boundary method with direct forcing for simulation of particulate flow. J. Comput. Phys. 209 (2), 448–476.

Wesseling, P., 2009. Principles of Computational Fluid Dynamics. 29 Springer Science & Business Media.

Yeo, K., Maxey, M.R., 2011. Numerical simulations of concentrated suspensions of monodisperse particles in a poiseuille flow. J. Fluid Mech. 682, 491–518.

Yu, Z., Wu, T., Shao, X., Lin, J., 2013. Numerical studies of the effects of large neutrally buoyant particles on the flow instability and transition to turbulence in pipe flow. Phys. Fluids (1994-present) 25 (4), 043305.

Zonta, F., Marchioli, C., Soldati, A., 2008. Direct numerical simulation of turbulent heat transfer modulation in micro-dispersed channel flow. Acta Mechanica 195 (1), 305–326.